Biophysical*Journal*
Article

Structure and Intermolecular Interactions between *L*-Type Straight Flagellar Filaments

Daniel Louzon,[1,2] Avi Ginsburg,[1,3] Walter Schwenger,[4] Tom Dvir,[1,2] Zvonimir Dogic,[4] and Uri Raviv[1,*]
[1]The Institute of Chemistry and the Center for Nanoscience and Nanotechnology, [2]The Racah Institute of Physics, and [3]The Institute for Drug Research, The Hebrew University of Jerusalem, Jerusalem, Israel; and [4]Department of Physics, Brandeis University, Waltham, Massachusetts

ABSTRACT Bacterial mobility is powered by rotation of helical flagellar filaments driven by rotary motors. Flagellin isolated from the *Salmonella Typhimurium* SJW1660 strain, which differs by a point mutation from the wild-type strain, assembles into straight filaments in which flagellin monomers are arranged in a left-handed helix. Using small-angle x-ray scattering and osmotic stress methods, we investigated the structure of SJW1660 flagellar filaments as well as the intermolecular forces that govern their assembly into dense hexagonal bundles. The scattering data were fitted to models, which took into account the atomic structure of the flagellin subunits. The analysis revealed the exact helical arrangement and the super-helical twist of the flagellin subunits within the filaments. Under osmotic stress, the filaments formed two-dimensional hexagonal bundles. Monte Carlo simulations and continuum theories were used to analyze the scattering data from hexagonal arrays, revealing how the bundle bulk modulus and the deflection length of filaments in the bundles depend on the applied osmotic stress. Scattering data from aligned flagellar bundles confirmed the theoretically predicated structure-factor scattering peak line shape. Quantitative analysis of the measured equation of state of the bundles revealed the contributions of electrostatic, hydration, and elastic interactions to the intermolecular forces associated with bundling of straight semi-flexible flagellar filaments.

INTRODUCTION

Bacterial locomotion is powered by rotating long ($\sim 10 - 15\ \mu$m), helical flagellar filaments, which are attached to the bacterial surface through a molecular motor embedded in the bacterial membrane. The complete flagellum-motor complex contains ~25 proteins. The flagellin homopolymer, however, comprises $>99\%$ of the flagellum length, providing the structural stiffness necessary to generate the thrust that powers bacterial motility (1,2). Each flagellar filament can be described as a helical assembly of flagellin protein monomers, with nearly 11 subunits per two turns of a one-start helix, or as a hollow cylinder comprising 11 protofilaments staggered in a nearly longitudinal helical arrangement (2,3). Each protofilament is a linear structure consisting of flagellin monomers stacked onto each other.

The flagellin monomers can exist in two distinct conformational states denoted as left-handed (*L*) or right-handed (*R*). Within each protofilament, all the monomers switch in a highly cooperative fashion, and thus, each protofilament also has either an *L* or an *R* configuration. If all the protofilaments within a single flagellum have the same conformational state, the entire assemblage assumes the shape of a straight hollow cylinder made of an *L* or *R* helical arrangement of the flagellin monomers (4). In many cases, however, a flagellum contains a mixture of *L* and *R* protofilaments, leading to a packing frustration that is resolved by the formation of a helical super-structure along the entire flagellum length, a unique feature that is essential for bacterial motility. Depending on the ratio of *R* to *L* filaments, there are a number of distinct structures of varying pitch and radius. In addition, point mutations in the flagellin amino acid sequence affect the helical structure (5). Flagellin mutants, in which all the protofilaments assume an *L* or an *R* conformational state, have been isolated and were shown to assemble into straight flagellar filaments (6,7). Another unique feature of flagella is that they can switch between different helical states in response to external stimuli, including ionic strength, pH, external forces, or temperature (3,8,9). Besides their obvious biological importance, their unique helical structure and intriguing stimuli-induced polymorphic transitions make flagella a highly promising, yet poorly explored, building block for assembly of soft materials and biologically inspired nano/micro machines (10).

To better understand bacterial taxis, which is driven by hydrodynamically bundled flagellar filaments, as well as

---

Submitted October 25, 2016, and accepted for publication February 6, 2017.

*Correspondence: uri.raviv@mail.huji.ac.il

Editor: Kazuhiro Oiwa.
http://dx.doi.org/10.1016/j.bpj.2017.02.038

to assemble flagellum-based soft materials, it is essential to elucidate the structure, as well as the intermolecular forces between flagellar filaments (11,12). Using small-angle x-ray scattering (SAXS), we investigated the behavior of *L*-type straight flagellar filaments isolated from the SJW1660 strain, which differs from the wild-type SJW1103 flagellin strain by the point mutation G426A. The structure of the flagellar filament was determined in solution. Under osmotic stress, the filaments formed bundles. To quantitatively model scattering patterns from flagellar bundles, we performed Monte Carlo simulations that accounted for the effect of thermal fluctuations on the arrangement of the filaments within the bundles. The line shape of the structure-factor correlation peak and the measured osmotic pressure-distance curves were consistent with theoretical predications (13,14). These experiments and models allowed us to determine the contributions of hydration, electrostatic, and elastic interactions to the equation of state describing the lateral forces acting between the flagellar filaments within the bundles and the bending stiffness of the filaments.

MATERIALS AND METHODS

Experimental

The *L*-type straight filament SJW1660, with flagellin point mutation G426A, was isolated from a mutant strain of the wild-type SJW1103 purified from *Salmonella enterica* serovar Typhimurium (15) according to a previously published protocol (10). Briefly, bacteria were grown to a log phase, sedimented at 8000 × *g*, and redispersed in a minimal volume by repeated pipetting with a 1 mL pipette. A very dense foamy bacterial solution was vortex mixed at the highest power setting for 5 min to separate flagella from the bacterial bodies (Genie 2 Vortex, Scientific Industries, Bohemia, NY). Subsequently, this suspension was diluted with a buffer and centrifuged at 8000 × *g* for 20 min to sediment bacterial bodies. The supernatant contained flagellar filaments, which were then concentrated by two centrifugation/resuspension steps at 100,000 × *g* for 1 h. For all experiments the flagella were resuspended in 100 mM NaCl and 10 mM K_2HPO_4 at pH 7, adjusted with a few mM of NaOH. To apply osmotic stress to the flagellar filaments and induce bundle formation, we used polyethylene glycol (PEG) of molecular mass 20 kDa (purchased from Sigma-Aldrich (St. Louis, MO) and used as received). Osmotic stress samples were prepared by mixing PEG and flagellar filament solutions, as described elsewhere (16–19). The osmotic pressure, Π, of each polymer solution was measured using a vapor pressure osmometer (Vapro 5520, Wescor, Pittsburgh, PA) and verified against the well-established (20) expression $\log \pi = a + b \times (wt\%)^c$, where $a = 1.57$, $b = 2.75$, and $c = 0.21$. Samples were first prepared in Eppendorf tubes, in which they were vortex mixed. Before SAXS measurements, each sample was transferred to a quartz capillary that was flame sealed and centrifuged at 6000 × *g*, using a Sigma 1-15PK centrifuge and rotor no. 11024, suitable for capillaries. The structural changes at each osmotic pressure were measured by SAXS.

Solution x-ray scattering data analysis

Most of the solution SAXS measurements were performed using our in-house setup. The x-ray source was a rotating anode MicroMax-007 HF (Rigaku, Tokyo, Japan) with a copper target, whose wavelength is 1.54 Å. The optics was a Confocal Max-Flux, CMF-12-100Cu8 focusing unit (Osmic, Rigaku). The detector was a MAR345 image plate (MarXperts, Norderstedt, Germany), the sample-to-detector distance was 1.8 m, and the exposure time was 2 h. The setup also includes scatterless slits (Forvis Technologies, Santa Barbara, CA) (21). More details about the setup are described in our earlier publication (22). Some of the data were measured at ID02 beamline at the European Synchrotron Radiation Facility. ID02 beamline optics consist of a cryogenic cooled Si-111 channel-cut monochromator and a focusing toroidal mirror. The beam size was 200 × 400 μm^2 (vertical and horizontal, respectively), with divergence of 20 × 40 μrad. The photon energy was 12.4 keV. The detector was a FReLoN 16M Kodak CCD, the sample-to-detector distance was 2 m, and the exposure time was 0.1 s. A more detailed description of the beamline characteristics is provided elsewhere (23).

To analyze the data, we simulated the real-space structure of the flagellar bundle and the interactions between neighboring filaments, and calculated the bundle's scattering intensity, *I*, as a function of q, which is the magnitude of the momentum transfer vector (or scattering vector), $\vec{q}$ (24–28). By comparing the simulation results with the data, we determined the structural parameters and physical properties of the bundles.

The initial estimate of structural parameters by the model was taken from electron cryo-microscopy data (29). The atomic structure (at 4 Å resolution) of an *L*-type flagellin monomer was taken from the Protein Data Bank (PDB: 3A5X) (15,30) and placed in a Cartesian coordinate system (Fig. 1). The origin was not placed at the subunit center of mass, but rather between the two α-helices at the z axis which points along the filament's long axis. This choice allowed a simpler relation between translations and rotations of the monomer with the filament axes. In particular, the scattering amplitude of atom i was calculated using the International Union of Crystallography (IUCR) atomic form factor:

$$f_i^0(q) = \sum_{j=1}^{4} a_j \exp\left(-b_j\left(\frac{|\vec{q}\,|}{4\pi}\right)^2\right) + c, \qquad (1)$$

where a_j, b_j, and c are the Cromer-Mann coefficients, given in Table 2.2B of the International Tables for X-ray Crystallography (31) and its subsequent corrections (32).

The scattering amplitude of the entire flagellin monomer is given by

$$F_{\mathrm{Monomer}}(\vec{q}) = \sum_j f_j^0(q) \cdot \exp\left(i\vec{q} \cdot \vec{r}_j\right), \qquad (2)$$

where $\vec{r}_j$ is the location of the jth atom in the monomer with respect to the origin, and $\vec{q}$ is the momentum transfer vector in reciprocal space. To

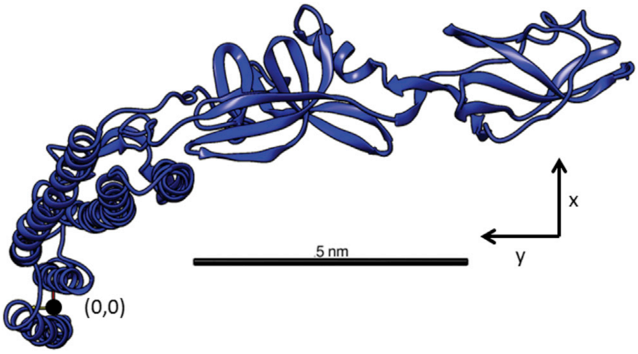

FIGURE 1 A 3D representation of the flagellin monomer, based on PDB: 3A5X (15). The coordinate system used in our computation model is indicated by the origin and the x and y axes, and the scale bar represents 5 nm. To see this figure in color, go online.

account for the contribution of the solvent, its displaced volume should be estimated (33–35). A uniform sphere (dummy atom) with a mean solvent electron density, ρ_0, and atomic radius, r_j^s, could have been placed at the center of each atom j in the PDB file. This approach, however, may generate errors at low q (36). Therefore, the uniform spheres were replaced by spheres with Gaussian electron density profiles (36),

$$\rho_j(\vec{r}) = \rho_0 \exp\left[-\left(\frac{\vec{r}}{r_j^s}\right)^2\right],$$

where ρ_0 is the mean electron density of the solvent ($\rho_0^{\text{water}} = 333(e/\text{nm}^3)$), and the r_j^s radii were published previously (33). When absent, empirical radii (37) were used. The scattering amplitude contribution of the Gaussian dummy atom is

$$F_j(\vec{q}) =$$

$$\int_0^{2\pi} d\phi_r \int_0^{\pi} d\theta_r \int_0^{\infty} \rho_0 \exp\left[-\left(\frac{r}{r_j^s}\right)^2\right] \exp[i\vec{q}\cdot\vec{r}]\, r^2 \sin\theta_r dr.$$

The result depends on the radius and q, owing to the spherical symmetry, and is given by

$$F_j(q) = \rho_0 \pi^{\frac{3}{2}} \left(r_j^s\right)^3 \exp\left[-\left(\frac{r_j^s q}{2}\right)^2\right]. \tag{3}$$

In this approach, the overall excluded volume, $V_{\text{ex}}^{\text{Gaussian}}$ is $\pi^{(3/2)}(r_j^s)^3$, and it is larger by a factor of $(3\sqrt{\pi}/4) \approx 1.33$ than the volume of the uniform sphere, $V_{\text{ex}}^{\text{Uniform}} = (4\pi/3)(r_j^s)^3$, in agreement with previous work (36). To better fit the data, the value of the mean electron density, ρ_0, was adjusted to some extent (Fig. S1). When the solvent contribution was taken into account, the scattering amplitude from a monomer became:

$$F_{\text{Monomer}}(\vec{q}) = \sum_j \left[f_j^0(q) - F_j(q)\right] \cdot \exp\left(i\vec{q}\cdot\vec{r}_j\right). \tag{4}$$

To describe the entire filament, we first translated the ith monomer, with respect to its origin reference point (Fig. 1), by the translation vector $\vec{R}_i(x_i, y_i, z_i)$. The monomer was then rotated by its Tait-Bryan (38) rotation angles, α_i, β_i, and γ_i, around the x, y, and z axes, respectively, using the rotation matrix

$$\mathbf{A}(\alpha,\beta,\gamma) = \begin{bmatrix} \cos\beta\cos\gamma & -\cos\beta\sin\gamma & \sin\beta \\ \cos\alpha\sin\gamma + \cos\gamma\sin\alpha\sin\beta & \cos\alpha\cos\gamma - \sin\alpha\sin\beta\sin\gamma & -\cos\beta\sin\alpha \\ \sin\alpha\sin\gamma - \cos\alpha\cos\gamma\sin\beta & \cos\gamma\sin\alpha + \cos\alpha\sin\beta\sin\gamma & \cos\alpha\cos\beta \end{bmatrix}.$$

The location and orientation of the ith subunit were described as

$$\begin{aligned} \alpha_i &= \beta_i = 0,\ \gamma_i = i \times \frac{4\pi}{NU} \\ x_i &= R\cos(\gamma_i),\ y_i = R\sin(\gamma_i),\ z_i = i \times \frac{P}{NU} \end{aligned}, \tag{5}$$

where R is the radius of the reference point, P is the two-pitch distance, and NU is the number of subunits in a two-pitch turn. Our model assumes that thermal fluctuations within each flagellum are negligible. Fig. 2 shows a two-dimensional (2D) projection of the helical lattice of the filament.

Using the reciprocal-grid (RG) algorithm (28), the flagella scattering form factor, FF, was numerically calculated,

$$FF(\vec{q}) = \sum_{i=1}^{n} F_{\text{Monomer}}\left(\mathbf{A}_i^{-1}(\alpha_i,\beta_i,\gamma_i)\cdot\vec{q}\right)\cdot\exp\left(i\vec{q}\cdot\vec{R}_i\right), \tag{6}$$

and orientationally averaged to give the solution scattering intensity,

$$I(q) = \frac{\int_0^{2\pi} d\phi_q \int_0^{\pi} \left|FF\left(q,\theta_q,\phi_q\right)\right|^2 \sin\theta_q d\theta_q}{\int_0^{2\pi} d\phi_q \int_0^{\pi} \sin\theta_q d\theta_q}, \tag{7}$$

where $\mathbf{A}_i$ and $\vec{R}_i$ are the rotation matrix and the translation vector, respectively, of the ith monomer.

Osmotic stress exerted by non-adsorbing polymers induced bundling of straight flagellar filaments. The scattering intensity owing to the packing of the flagellar filaments was computed using the form factor of a single filament, FF, as a unit cell. The form factor was multiplied by a structure factor (lattice sum), $SF(\vec{q})$, of a 2D lattice and orientationally averaged, $\langle FF(\vec{q})\cdot SF(\vec{q})\rangle$, in $\vec{q}$-space. We assumed a perfect hexagonal 2D lattice as our starting point (Fig. S5). This assumption is equivalent to assuming that the chains are very stiff. The fitting parameters of a hexagonal lattice were the spacing between the centers of neighboring filaments, a, and the domain size (the distance over which two lattice points maintain positional correlation). These parameters determined the position and width of the correlation peaks in the scattering intensity. Since samples were in solution at room temperature, the lattice exhibited significant thermal fluctuations, which washed away the sharp peaks of the structure factor (Fig. S5).

In real space, a finite 2D lattice, at zero temperature, is described by

$$SF_r(\vec{r}) = \delta(z)\sum_i^M \delta(x - x_i)\delta(y - y_i), \tag{8}$$

where $\vec{r}_i = (x_i, y_i, z_i)$ is the location of the ith point in a lattice with M unit cells. At a finite temperature, thermal fluctuations work against the intermolecular forces, affecting the lattice structure. Assuming a harmonic potential between nearest neighbors, we calculated the pairwise energetic cost, ΔE_i, for a small displacement, $\Delta\vec{r}$, of the ith lattice point from its mean location, $\vec{r}_i$, at a given temperature:

$$3\Delta E_i = \tfrac{1}{2}\kappa \sum_{j\in nn} \left[\left(\vec{r}_{\perp i} + \Delta\vec{r}_{\perp} - \vec{r}_{\perp j}\right)^2 - \left(\vec{r}_{\perp i} - \vec{r}_{\perp j}\right)^2\right]. \tag{9}$$

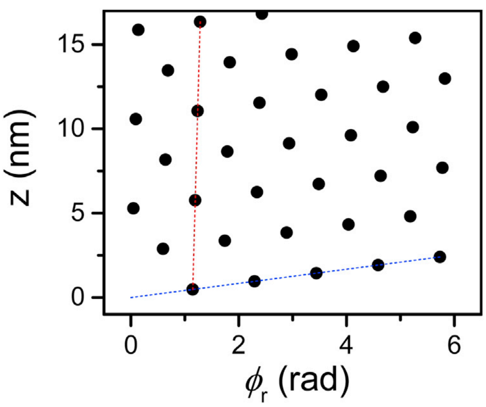

FIGURE 2 A projection of the helical lattice showing the monomer axial rise, z (0.48 ± 0.01 nm per monomer), and the packing arrangement at the radius of the reference point ($R = 2.42 \pm 0.02$ nm). The dotted red line shows the shift between monomers that are on top of one another. The dotted blue line shows the axial rise between adjacent monomers. $\phi_r = \gamma_i \bmod 2\pi$, where γ_i is defined in Eq. 5. To see this figure in color, go online.

Here, $\vec{r}_{\perp i} = (x_i, y_i, 0)$ and nn denote nearest neighbors and κ is the lattice elastic constant between neighbors. The factor of 3 accounts for the fact that on average, each chain has six neighbors and the interaction is shared between the interacting pairs (39). The probability of a deviation, ΔE_i, in the energy is

$$P_i(\Delta E_i) \sim \exp\left(-\frac{\Delta E_i}{k_B T}\right), \tag{10}$$

where k_B is the Boltzmann constant and T is the absolute temperature. To estimate the effect of thermal fluctuations, we performed Monte Carlo simulations. In each iteration, we tested the probability of a random displacement at a random lattice point against a random number between 0 and 1. If the random number was smaller than the calculated probability, $P_i(\Delta E_i)$, the displacement was accepted. Repeating this process for ~10^9 iterations, using periodic boundary conditions, converged into a stable, slightly (depending on the value of κ) disordered 2D hexagonal lattice. Fig. S6 shows how the value of κ affected the calculated intensity in this model.

In real space, the total electron density is a convolution of the electron density of a filament, $\rho_{\text{filament}}(\vec{r})$, and the 2D bundle lattice, $SF_r(\vec{r})$. In reciprocal space, the convolution becomes a multiplication; hence, the total scattering amplitude is

$$F(\vec{q}) = FF(\vec{q}) \cdot SF(\vec{q}), \tag{11}$$

where

$$SF(\vec{q}) = \sum_{i=1}^{M} \exp(i\vec{q} \cdot \vec{r}_i). \tag{12}$$

To obtain the scattering intensity, $I_{\text{bundle}}(q)$, we calculated the square of the scattering amplitude, $\left|F(q, \theta_q, \phi_q)\right|^2$, and averaged over all the orientations in reciprocal space (θ_q and ϕ_q), as in Eq. 7 (28). $I_{\text{bundle}}(q)$ was then compared with the experimental SAXS data.

RESULTS AND DISCUSSION

Scattering from flagellar suspensions

The x-ray scattering 2D pattern from a dense solution of straight flagella, isolated from strain SJW 1660, was azimuthally averaged, yielding an experimental scattering intensity curve (Fig. 3). The experimental data were compared with the scattering curve computed from a flagellar model in which the atomic structure of flagellin monomers (Fig. 1) was arranged on a flagellar one-start left-handed helical lattice. The relevant microscopic parameters in Eq. 5 (R, P, and NU) were varied to obtain the best fit of our theoretical computed curve to the experimental scattering data and to estimate the error in the form-factor fitting parameters (Figs. S2–S4). During this procedure, the atomic structure of the flagellin subunit, obtained from PDB: 3A5X (15), was preserved and the subunits were not allowed to overlap.

In our experiments, the average length of flagellar filaments was 4 ± 2 μm (10). The SAXS measurements, however, were insensitive to objects longer than a few hundred nanometers; hence, in our theoretical computations, the filament length, L, was fixed at 300 nm (in other words, the filament contained $n = 660$ monomers). Models with longer filaments required more computational resources and did not change the scattering intensity profile, or better fit the data, in the q-range of our data. A quantitative comparison of experimental measurements to the theoretical model

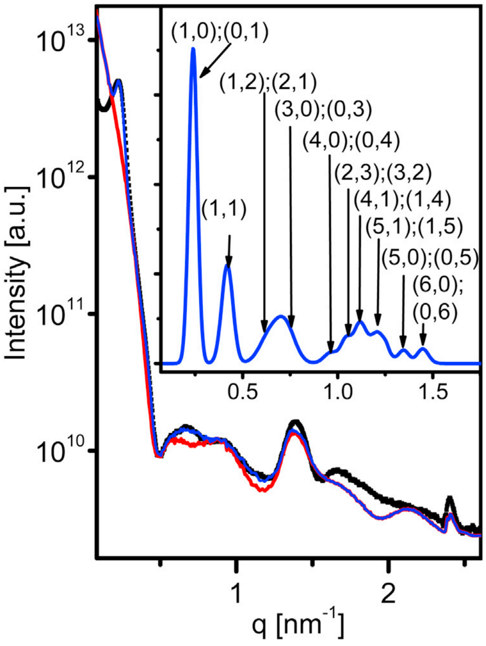

FIGURE 3 Azimuthally integrated scattering intensity as a function of q (the magnitude of the momentum transfer vector, $\vec{q}$), from isotropic solution of the SJW1660 strain in 100 mM NaCl (*black solid squares*). The form factor (*red curve*) of a flagellar filament was computed using Eqs. 2 and 7 and fitted to experimental data yielding the following essential flagellar structural parameters: filament diameter, $D = 23.1$ nm; two-turn pitch, $p = 5.2$ nm; 10.96 flagellin subunits per two-turn pitch; and the radius of the reference point, $R = 2.42$ nm. The blue curve corresponds to the same form factor when multiplied by the structure factor of a 2D hexagonal phase with a lattice constant, a, of 30.0 nm. The structure factor and its peak indexes are shown in the inset. To see this figure in color, go online.

revealed a filament diameter, D, of 23.1 ± 0.1 nm, a two-turn pitch, P, of 5.2 ± 0.1 nm, $NU = 10.96 \pm 0.01$ flagellin subunits/two-turn pitch, and a radius of the reference point, R, of 2.42 ± 0.02 nm (Fig. 4). These values are consistent with electron cryo-microscopy and x-ray fiber diffraction data ($D = 23 - 24$ nm (30,40), $P = 5.27$ nm, $NU = 11.26$ (15,40), and $R = 2.5$ nm (15)).

Using Gaussian dummy atoms (Eqs. 4 and 7) to account for the contribution of the solvent with reasonable values for the solvent electron density, ρ_0 (in Eq. 3), did not significantly improve the fit of our form-factor model to the experimental data (Fig. S1). The contribution of the solvent was therefore not computed in subsequent models (in other words, Eqs. 2 and 7 were used). By varying the model parameters, we determined the effect of each parameter on the locations and magnitudes of various features in the calculated intensity. The first minimum was mainly controlled by the flagellar filament diameter (see Fig. S2), the peak at $q = 1.4\ \mathrm{nm}^{-1}$ was closely associated with the helical pitch (see Fig. S3), and the peak at $q = 2.4\ \mathrm{nm}^{-1}$ was attributed to the axial rise (Fig. S4). The high sensitivity of our model to these structural parameters and their weak interdependency is demonstrated in Figs. S2–S4.

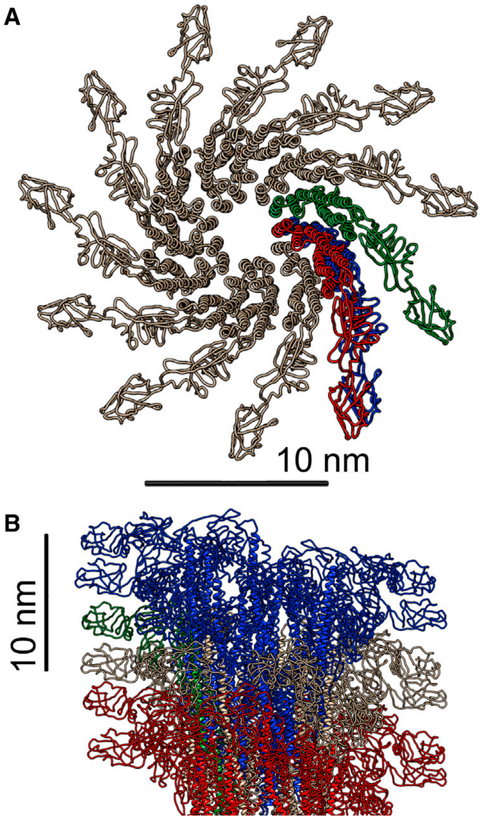

FIGURE 4 3D atomic model of a two-turn pitch (11 flagellin subunits). (A) Top view. (B) Side view of a three-pitch filament along the filament long axis. The blue subunit is the first monomer (at $z = 0$), and the red subunit is the monomer unit of the second two-turn pitch, which is slightly shifted (see Fig. 2). To see this figure in color, go online.

To obtain high signal/noise scattering patterns, we used a 27 ± 0.1 mg/mL (or 0.524 ± 0.002 mM) flagellar suspension. Based on the structure of the flagellar filaments, the mean filament volume fraction, ϕ, in this sample was $\simeq 0.062$. Previous work has demonstrated that rigid rods form a nematic phase when $(\phi L/D) > 4$. This relationship becomes quantitatively valid in the Onsager limit in which $L/D > 100$ (41,42). Consequently, because our flagellar filaments were $>2\ \mu$m, and thus satisfied the Onsager criterion, the filament suspension formed nematic liquid crystals. We note that inherently, polydispersity of flagellar filaments significantly widens isotropic-nematic co-existence. This makes it possible that shorter filaments partitioned into an isotropic phase (43). Furthermore, rigorous analysis would have to account for the contribution of electrostatic repulsion, which leads to an effective diameter that can be significantly larger than the bare one. The high ionic strength of our suspension, however, significantly reduced this contribution (44).

Although the majority of the measured scattering pattern from flagellar filaments is owing to the form factor, the signal also contained weak structure-factor correlation peaks, at $q_{(1,0)} = 0.24\ \mathrm{nm}^{-1}$ and its higher harmonics (Fig. 3). The presence of these peaks suggests that a fraction of the filaments within our sample formed hexagonal bundles with a lattice constant, a, of 30.0 ± 0.1 nm (Fig. 3, *inset*). Within such bundles, the volume per chain is $(\sqrt{3}La^2/2)$, where L is the mean filament length. The volume of a chain is $(L\pi D^2/4)$; hence, the volume fraction of the filaments in our lattice, given by the ratio of the two, $\phi = (\pi D^2/2\sqrt{3}a^2)$, was $\simeq 0.54$. The average volume fraction of the filaments, however, was $\simeq 0.062$, suggesting that a low-density nematic liquid crystal coexisted with a low fraction of filaments that formed high-density hexagonal bundles.

Lindemann stability criterion asserts that the root mean-square displacement (RMSD), $\langle|\vec{u}\,|^2\rangle^{(1/2)}$, in a lattice should be small compared with the lattice constant ($<0.1a$). In a lattice with purely steric interactions (13),

$$\langle|\vec{u}\,|^2\rangle^{\frac{1}{2}} = 3^{\frac{1}{2}}(a - D). \tag{13}$$

The lattice is expected to melt when $a_{\max} \approx 1.2D$, which in the case of our flagellar filaments corresponds to $a \approx 28$ nm (13). For the filaments in the hexagonal phase, a was $\approx 1.3D$, suggesting that the van der Waals attractive interactions between the filaments were not negligible and stabilized the bundle structure. The structure-factor peaks were relatively wide (with a full width at half-maximum of $\approx 0.06\ \mathrm{nm}^{-1}$), suggesting that the hexagonal bundles had small lateral dimensions. Applying Warren's approximation revealed that, on average, there were only ~ 3 filaments that maintained positional correlation in the lattice (45).

Measuring the equation of state for flagellar solutions using the osmotic stress technique

To induce large-bundle formation, we applied osmotic stress to the flagellar filaments by adding increasing concentrations of an inert polymer (PEG: molecular mass, 20 kDa) to our SJW 1660 flagellar filament solution (Fig. 5). We then determined the structure of the forming flagellar filament bundles and the interactions between filaments in the bundles. To obtain the mean interfilament lateral separation, a, and the average coherence length, along which the positional order of filaments within the bundle is maintained, we modeled the scattering from a filamentous bundle and compared it with experimental measurements (Fig. 5 *B*). We multiplied the single-filament form factor (Eq. 6) by a hexagonal lattice sum (Eqs. 11 and 12) and orientation averaged the product in $\vec{q}$-space (Eq. 7). To take into account the effect of thermal fluctuations, we assumed a harmonic potential between nearest-filament neighbors and calculated the energetic cost of random small displacements in the hexagonal lattice (Eq. 9). We performed Monte Carlo simulation (using Eq. 10) that equilibrated the lattice structure. A lattice of 40×40 with $\kappa = 1.2 \pm 0.1\ \mathrm{mN \cdot m^{-1}} = 0.29 \pm 0.02\ \mathrm{k_B T \cdot nm^{-2}}$ (κ is defined in Eq. 9) was kept constant. Based on the locations of the filament centers that were obtained from the simulations, we calculated the structure factor (Eq. 12) and $I_{\mathrm{bundle}}(q)$ (Eq. 7), and compared these predictions with the experimental SAXS data.

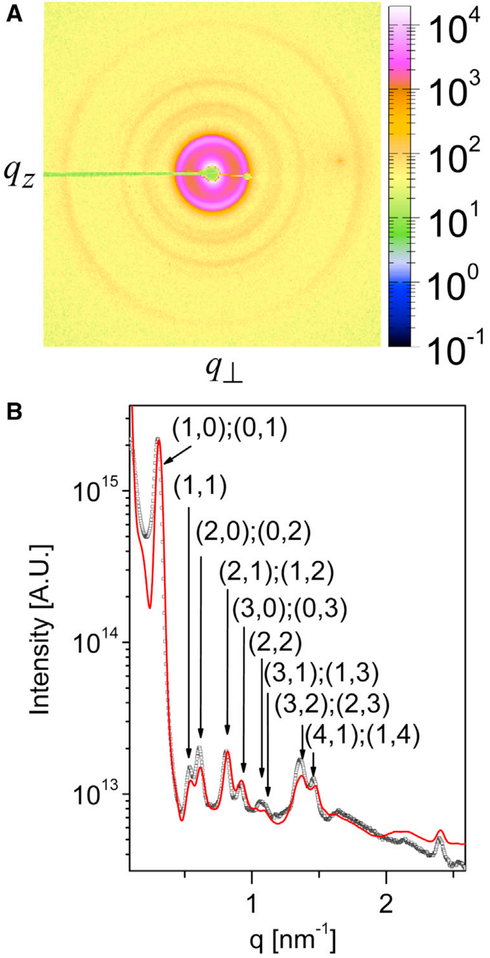

FIGURE 5 Scattering from an isotropic suspension containing bundles of SJW1660 straight flagellar filaments in 100 mM NaCl. The bundles were assembled using a 5 wt % PEG (molecular mass, 20 kDa) concentration, corresponding to an osmotic pressure of 47 kPa (20). (*A*) Two-dimensional x-ray scattering image. (*B*) Azimuthally integrated scattering intensity as a function of q. The experimental measurements (*black squares*) were fitted to our computational hexagonal lattice model (*red curve*) with a lattice constant of $a = 23.5$ nm. Good agreement can be seen over a wide q-range in both the location and magnitude of the peaks, whose indexes are indicated in brackets. To see this figure in color, go online.

Three lattice parameters affected the scattering intensity, $I_{\mathrm{bundle}}(q)$: 1) the 2D hexagonal lattice size, a, which determined the locations of the structure-factor correlation-peak centers (Fig. S7); 2) the lattice coherence length (i.e., the positional correlation length of the lattice), which mainly influenced the width of the structure-factor correlation-peaks (Fig. S8); and 3) the elastic constant, κ, which affected the intensity and number of structure-factor peaks (Fig. S6). High κ values correspond to weaker thermal fluctuations and, hence, sharper correlation peaks. Our computational model quantitatively fitted the experimental scattering curve over a wide range of q values (Fig. 5 *B*). Results for other osmotic pressures, which show comparable agreement with the computational model, are shown in Fig. S9. From the equipartition theorem and the value of κ, we can estimate the RMSD of a single flagellar chain confined in the hexagonal lattice to be (39) $\langle |\vec{u}|^2 \rangle^{(1/2)} = \sqrt{(k_B T/\kappa)} = 1.85 \pm 0.08$ nm.

Taking into account hydration repulsion, the bending stiffness, κ_s, of the flagellar filaments, and the electrostatic interactions between them, the equation of state for a bundle of long semi-flexible chains like DNA in solution is (14)

$$\frac{\partial G}{\partial d}(d) = \frac{\partial H_0}{\partial d}(d) + c k_B T \kappa_s^{-\frac{1}{4}} \frac{\partial}{\partial d} \sqrt[4]{\frac{\partial^2 H_0}{\partial d^2}}, \tag{14}$$

where G is the free energy, $d = a - D$ is the spacing between filaments, κ_s is the bending stiffness, H_0 is

$$H_0(d) = a_h \frac{e^{-d/\lambda_H}}{\sqrt{d/\lambda_H}} + b \frac{e^{-d/\lambda_D}}{\sqrt{d/\lambda_D}}, \tag{15}$$

where λ_H and λ_D are the hydration and electrostatic screening lengths, respectively. The explicit expression of $(\partial G/\partial d)(d)$ is given in Section S6 in the Supporting Material.

In a hexagonal lattice, the relation between the free energy and the osmotic pressure is (14)

$$\Pi(d) = -\frac{1}{\sqrt{3}d} \frac{\partial G}{\partial d}(d). \tag{16}$$

As expected, the lateral filament spacing, a, obtained from fitting the scattering data to our model (as demonstrated in Fig. 5) decreased with increasing osmotic pressure (Fig. 6). The experimental pressure-distance curve could be quantitatively fitted to the theoretical equation of state (Eqs. 14–16). We fixed the filament hard-core diameter, D, to the value obtained from the form-factor analysis (23 nm) when performing the fit. The fit yielded the parameters $a_{\mathrm{h}} = 40 \pm 5\ \mathrm{Pa} \cdot \mathrm{nm}^2$, $b = 40 \pm 5\ \mathrm{Pa} \cdot \mathrm{nm}^2$, $c = 1.7 \pm 0.1$, $\kappa_{\mathrm{s}} = 2.9 \pm 0.4 \cdot 10^{-15}\ \mathrm{J} \cdot \mathrm{nm}$, $\lambda_{\mathrm{H}} = 0.26 \pm 0.03$ nm, and $\lambda_{\mathrm{D}} = 0.82 \pm 0.03$ nm. λ_{H} is close to the expected value of ~3 Å (46). λ_{D} can be calculated from the calculated ionic strength of the sample, 0.84 nm (47). The small difference between the calculated and the measured λ_{D} could be explained by the small amount of NaOH that was added to the solution to maintain natural pH. We kept the value of the prefactor c close to unity, as obtained in an earlier study (14). a_{h} and b were first fitted to the high-pressure data, where the contribution of the hydration and electrostatic forces should dominate.

The bending stiffness, κ_{s}, terms dominated the lower pressure data and are associated with the persistence length of the filaments (13): $P = (k_{\mathrm{s}}/k_{\mathrm{B}}T) = 700 \pm 100\ \mu\mathrm{m}$. This value is significantly higher than the persistence length of actin (18 μm), which has a smaller cross section, and comparable to the persistence length of a taxol-free microtubule (700–1500 μm), which has a slightly larger cross section (48). A taxol-stabilized microtubule has, as expected, a longer persistence length (5200 μm) (48). The latter values were measured from thermal fluctuations in the shape of the filaments. Note that the persistence length that we found is higher than the value determined from electron micrographs of isolated, negatively stained filaments (41 μm) (11). Finally, a constant weak negative effective pressure of 37 Pa was added to account for the contribution of the van der Waals interaction, which led to the hexagonal phase when no osmotic stress was applied (Fig. 3).

Whereas the theoretical model quantitatively fits the data over a wide range of applied osmotic pressures, when the filaments were far apart, the model (Eq. 14) predicted a slightly more repulsive interaction than measured. At very high pressures (490 kPa or higher), the filaments assumed lattice-spacing values, a, that were smaller than the unstressed filament diameter. Our data, however, show that at these high pressures, the first minimum of the azimuthally integrated scattering curve moves toward higher q values, suggesting that the form factor has changed owing to deformation of the filaments (Fig. 7). This change is consistent with a tighter monomer packing resulting in a smaller filament diameter, D. From the structure of the flagellar filaments we can calculate the cross-section geometrical moment of inertia, $I \approx (\pi/4)[(D/2)^4 - R^4] = 1.4 \times 10^4\ \mathrm{nm}^4$. The filament Young's modulus, E, is then given by (48)

$$E = \frac{P}{I} \approx 0.20 \pm 0.03\ \mathrm{GPa},$$

where we have assumed that $P = 700 \pm 100\ \mu\mathrm{m}$. Table 1 summarizes the parameters determined in this study.

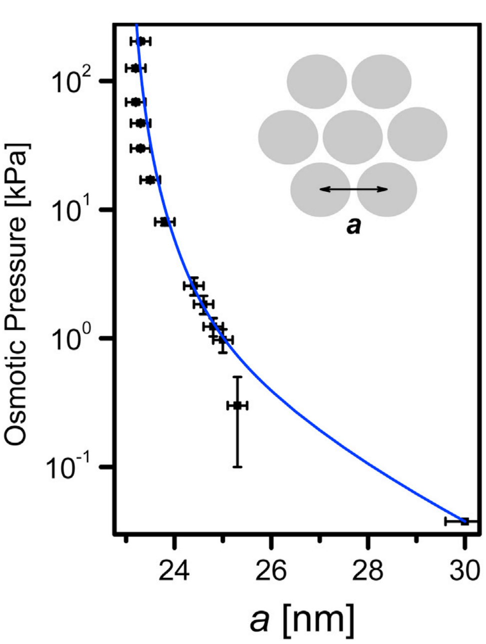

FIGURE 6 The equation of state of bundled straight filaments shows how the lattice constant, a, of a hexagonal bundle (see inset for a schematic *top view*) of straight filaments depends on the applied osmotic pressure. The blue curve indicates the fit of the theoretical model (Eq. 14) to the data. To see this figure in color, go online.

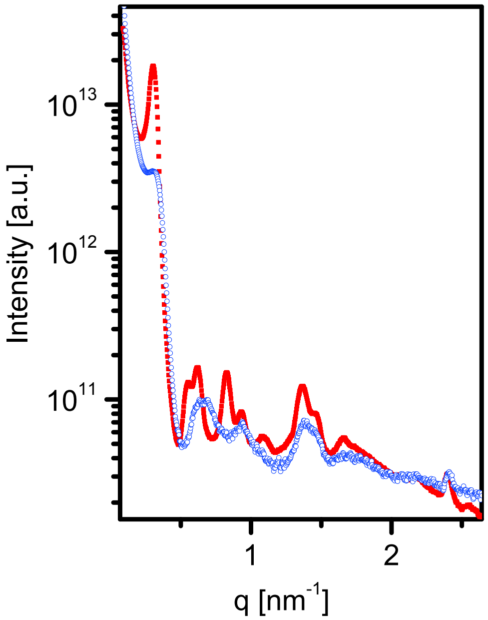

FIGURE 7 At high osmotic pressures, the scattering profiles exhibited a discontinuous change indicating a structural change of the constituent flagella. A comparison between SAXS patterns measured for moderate (30 kPa; *red solid symbols*; hexagonal lattice spacing, 23.3 nm) and high (490 kPa; *blue open symbols*; hexagonal lattice spacing, 21 nm) osmotic pressures. To see this figure in color, go online.

TABLE 1 Summary of the Parameters Determined In This Study

Parameter Name, Symbol	Value	Error	Units
Filament diameter, D	23.1	0.1	nm
Two-turn pitch, P	5.2	0.1	nm
Radius of the reference point, R	2.42	0.01	nm
Number of flagellin subunits per two-turn pitch, NU	10.96	0.01	
Hexagonal lattice elastic constant between neighbors, κ	1.2	0.1	$\mathrm{mN \cdot m^{-1}}$
RMSD of a flagellar chain in the hexagonal lattice, $\langle\lvert\vec{u}\rvert^2\rangle^{(1/2)}$	1.85	0.08	nm
Flagellar bending stiffness, κ_s	2.9	0.4	10^{-15} J • nm
Flagellar Young's modulus, E	0.20	0.03	GPa

Within the hexagonal lattice, semi-flexible flagellar filament chains are confined to an effective "tube" within the hexagonal lattice. It has been argued that fluctuations of this type of confined filaments can be described by a single characteristic length scale, which points along the long axis, $\hat{z}$, direction of the filaments. This length scale is the Odijk deflection length, λ_{def}, which is the average displacement between successive collisions along the chain within the confined lattice and is given by (49,50)

$$\lambda_{\mathrm{def}} \approx P^{\frac{1}{3}} d^{\frac{2}{3}}. \tag{17}$$

Equation 17 is based on scaling theory and agrees well with Monte Carlo simulations up to a prefactor of order 2 (51). The mean fluctuations in the nematic director can then be estimated from the deflection length (13):

$$\left\langle \lvert n_{\perp}\rvert^2 \right\rangle \approx \left[\frac{d}{\lambda_{\mathrm{def}}}\right]^2. \tag{18}$$

Therefore, it follows that the measurement of d directly yields the Odijk deflection length.

The bulk modulus,

$$B \equiv -V\frac{d\Pi}{dV}, \tag{19}$$

can be computed from the theoretical $\Pi(d)$ (Eq. 16). The compressed volume, V, is taken to be the volume of solution per chain inside the hexagonal lattice (52) and is given by $V/L = (\sqrt{3}a^2/2) - \pi(D^2/4) \equiv A_c$, where L is the chain length and A_c is the compressed area per chain. Assuming that L remained unchanged under the osmotic pressures applied in our experiment, $dV = L \cdot dA_c$, $B = -A_c(d\Pi/dA_c)$ and is independent of L. Using the above formula we can determine how the calculated bulk modulus, deflection length, and mean fluctuations in the nematic director vary with the lattice spacing, a (Fig. 8). The bulk modulus decreased with a, whereas the deflection length and the mean fluctuations in the nematic director increased with a.

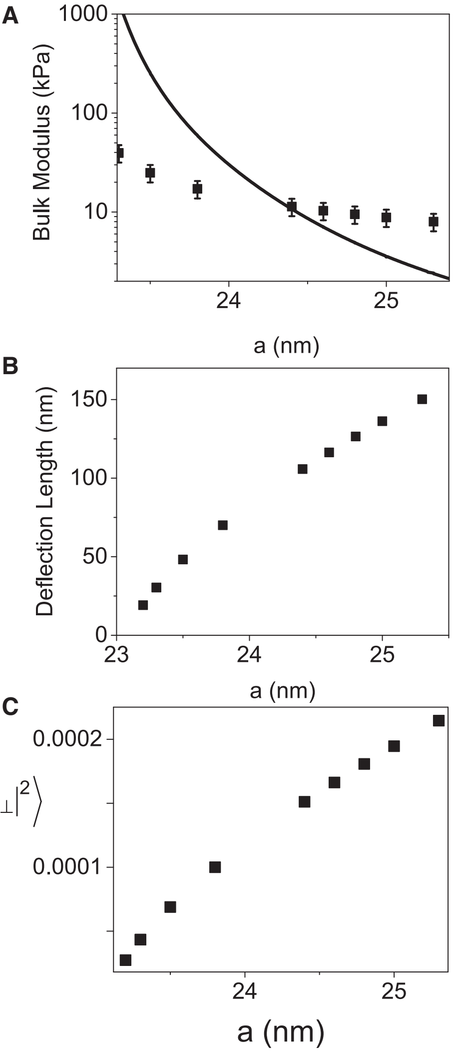

FIGURE 8 Elastic constants of the hexagonal phase as a function of the lattice spacing, a. (*A*) The bulk modulus, calculated based on the osmotic stress data (*solid curve*) or on the Monte Carlo simulation results (*solid symbols*). (*B*) The deflection length (the average displacement between successive collisions along the chain within the confined lattice). (*C*) The fluctuations in the nematic director. To see this figure in color, go online.

The bulk modulus can also be estimated from κ by scaling analysis. To obtain units of pressure, κ should be divided by a length scale. The relevant length scale in this case is the deflection length, λ_{def}, which is the length scale over which the displacement of the filament is kept within the tube around the filaments, which is in the original lattice site. Hence, we obtain

$$B \approx \frac{\kappa}{\lambda_{\mathrm{def}}}. \tag{20}$$

Fig. 8 confirms that the bulk modulus, which was estimated from the Monte Carlo simulations by scaling analysis (Eq. 20), yields bulk moduli that are of the same order of magnitude as those obtained from the osmotic stress data (Eq. 19).

When a was smaller than ~23.5 nm, the scaling analysis deviated from the bulk modulus, which was computed from the osmotic stress data. The deviation might be attributed to the fact that as a gets shorter, κ might change (13); hence, Eq. 20 does not provide a good estimate of B at low a values.

Twist of the flagellar bundle could have contributed to disorder in the bundles (53). Twist distortions, however, are expected to occur on length scales of the filament curvature, which in our case was much longer than the accessible length scale in our SAXS experiments.

Scattering from aligned flagella samples

In most of our samples, the solutions were isotropic, as demonstrated in the 2D scattering pattern shown in Fig. 5 *A*. In a few samples, however, without any special treatment (54–56), we accidentally obtained 2D scattering images from partially aligned bundles of SJW1660 filaments. These data were taken at the ID02 beamline, European Synchcrotron Radiation Facility (Grenoble, France). The 2D scattering data showed local bundle alignment, owing to the flow of the high bundle concentration in the narrow (~2 mm) quartz flow-cell capillary (Fig. 9). The 2D structure-factor peaks, associated with lateral packing, were located along the perpendicular axis, $q_\perp$. The peak at 1.4 nm^{-1}, attributed to the two-turn helical pitch, was along a diagonal line situated between the vertical (q_z) and horizontal $(q_\perp)$ axes, and the peak at 2.4 nm^{-1}, which shows the helical axial rise, was along the vertical, q_z, axis, as expected.

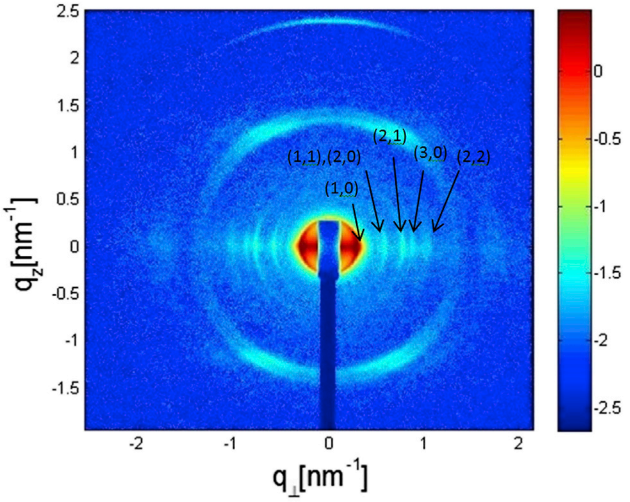

FIGURE 9 2D x-ray scattering image from a partially aligned bundle of straight filaments. The filaments were aligned along their long, z, axis. Using Cartesian coordinates in reciprocal space, the scattering vector, $\overrightarrow{q}$, has three components, q_x, q_y, and q_z. On a 2D detector, we can observe the q_z component and the $q_\perp$ component, which is the projection of the scattering vector on the (q_x, q_y) plan and is given by $q_\perp = \sqrt{q_x^2 + q_y^2}$. To see this figure in color, go online.

To calculate the structure factor, $S(q_\perp, q_z)$, both the density, $\rho(\vec{r})$, and the local displacement field, $u(\vec{r})$, should be evaluated. $u(\vec{r})$ was calculated from the elastic free energy for fluctuations in the hexagonal phase (13). $\langle|\vec{u}|^2\rangle^{(1/2)}$ is directly related to the stability of the hexagonal bundle (in other words, the lattice is unstable when $\langle|\vec{u}|^2\rangle^{(1/2)}$ diverges).

By alignment of the filaments in the flow-cell capillary we obtained 2D scattering data from the hexagonal flagellar bundles that we could compare with the theoretical structure factor calculated for semi-flexible long chains (13). The model, which takes into account the elastic free energy of undulations in a hexagonal phase of chains, predicts that the line shape of the hexagonal structure-factor peaks should decay as power laws in the tails of the peaks. In particular, for the $(1,0)$ and $(0,1)$ peaks, the data contained enough points to confirm the predicted power lows. Fig. 10 *A* presents a log-log plot of the $(1,0)$ peak along the perpendicular direction, $q_\perp$, with a linear fit, using a slope of -2.0 ± 0.1, confirming the predicated (13) structure-factor line shape of: $SF(q_\perp - G_{(1,0)}, q_z = 0) \propto q_\perp^{-2}$, where $G_{(1,0)}$ is the $(1,0)$ peak center. Fig. 10 *B* presents a log-log plot of the $(0,1)$ peak along the vertical, q_z, axis using a linear fit with a slope of -4.0 ± 0.1, confirming the predicted structure-factor line shape of $SF(q_\perp = 0, q_z - G_{(0,1)}) \propto q_z^{-4}$, where $G_{(0,1)}$ is the center of the $(0,1)$ peak. Similar structure-factor line shapes can be expected for other semi-flexible filament bundles, including microtubule or neurofilament bundles (57).

CONCLUSIONS

We have used solution SAXS to determine the structure of the L-type straight flagellar filament strain SJW 1660. Using the atomic model of the flagellin subunit, we calculated the scattering curve from the helical lattice of the entire filament and compared with our scattering data. We found that the helix had a diameter of 23.1 ± 0.1 nm, a two-turn pitch of 5.2 ± 0.1 nm, and 10.96 ± 0.01 flagellin subunits/two-turn pitch. Under osmotic stress, the filaments formed 2D hexagonal bundles. To fit the solution x-ray scattering curves of 2D hexagonal bundles, Monte Carlo simulations were used to account for thermal fluctuation effects and the interactions between filaments in the bundles, assuming harmonic pairwise potentials between neighboring filaments with an elastic constant, κ, of 1.2 ± 0.1 $\text{mN} \cdot \text{m}^{-1}$. We determined the distance between the semiflexible flagellar filaments in the bundles as a function of osmotic stress. We could fit the resulting pressure-distance curve to the equation of state of hexagonal bundles of semi-flexible chains like DNA (14), from which the parameters associated with the electrostatic, hydration, and undulation interactions were determined. The undulation energy was associated with a bending stiffness, which corresponds to a chain persistence length of $\approx 700 \pm 100$ μm. Table 1 summarizes the parameters determined in this study.

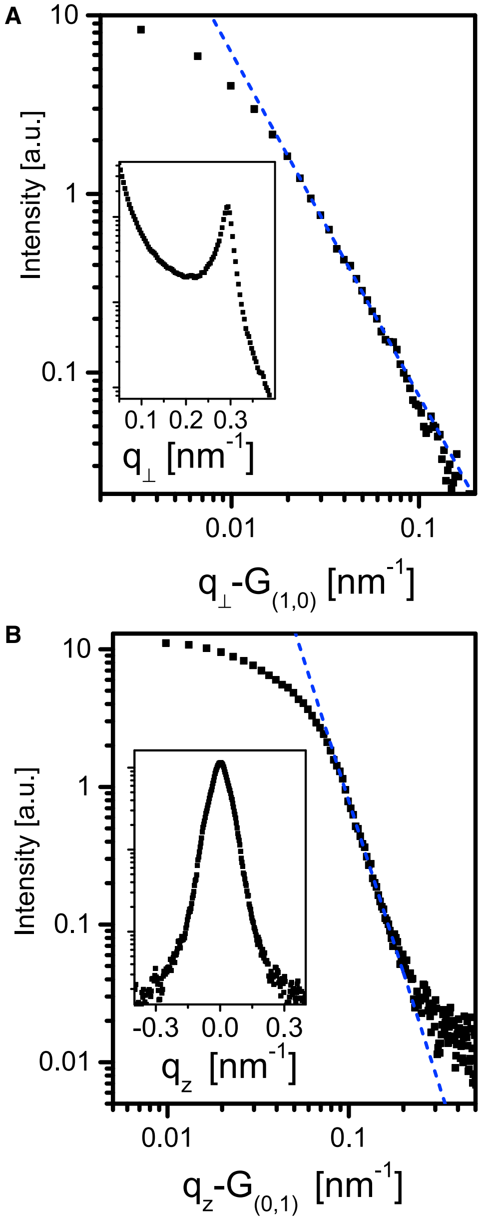

FIGURE 10 (*A*) A log-log plot of the (1,0) peak tail (*solid symbols*) along $q_\perp$, showing a linear tail. $G_{1,0}$ is the peak center. The broken line is a linear fit with a slope of -2.0 ± 0.1, as theoretically predicted (13). The inset shows the shape of the peak on a log-linear scale. (*B*) A log-log plot of the (0,1) peak tail (*solid symbols*) along q_z, averaged over 5 pixels in $q_\perp$, showing a linear tail. The center of the peak is at $G_{0,1}$. The broken line is a linear fit with a slope of -4.0 ± 0.1, as theoretically predicted (13). The inset shows the shape of the peak on a log-linear scale. To see this figure in color, go online.

We then computed the bundle bulk modulus, the deflection length of the filaments within the bundle, and the mean fluctuations in the nematic director, as well as the variation of these parameters with the hexagonal lattice spacing. Using scaling arguments, we confirmed that the bundle bulk modulus obtained from the Monte Carlo simulations is in agreement with the bulk modulus obtained from the osmotic stress data. Furthermore, the tails of the bundle structure-factor peak line shapes followed the theoretically predicted (13) power-law behavior (for semi-flexible chains) with exponents of -2 and -4 in the perpendicular and axial directions, respectively. The persistence length of flagellar filaments is similar to that of a microtubule. However, owing to the larger microtubule lumen, osmotic stress deforms the microtubule at low pressures. Higher pressures lead to 2D hexagonal bundles like those of DNA and flagella (14,17,18). The stiffness of the flagellar filaments is important for bacteria to swim efficiently using propeller-like beating motions of these filaments.

SUPPORTING MATERIAL

Supporting Materials and Methods and nine figures are available at http://www.biophysj.org/biophysj/supplemental/S0006-3495(17)303253-9.

AUTHOR CONTRIBUTIONS

D.L., W.S., Z.D., and U.R. designed research; D.L., A.G., T.D., W.S., Z.D., and U.R. performed research; D.L., A.G., T.D., and U.R. contributed analytic tools; D.L., Z.D., and U.R. analyzed data; D.L., Z.D., and U.R. wrote the manuscript.

ACKNOWLEDGMENTS

We thank Daniel Harries and Daniel J. Needleman for helpful discussions. We acknowledge the European Synchrotron Radiation Facility for providing access to their synchrotron radiation facilities, and we thank T. Narayanan and G. Lotze for assistance in using beamline ID02, as some of our data were acquired there.

D.L., A.G., T.D., and U.R. acknowledge financial support from the Israel Science Foundation (grant 1372/13), US-Israel binational Science Foundation (grant 2009271), Rudin, Wolfson, and Safra Foundations, and the FTA-Hybrid Nanomaterials program of the Planning and Budgeting Committee of the Israel Council of Higher Education. D.L. and T.D. thank the Center for Nanoscience and Nanotechnology of the Hebrew University for fellowships. A.G. thanks the Institute for Drug Research at the Hebrew University for a fellowship. Z.D. and W.S. acknowledge support from the National Science Foundation through grants DMR-CMMI-1068566, NSF-DMR-1609742, and NSF-MRSEC-1420382. We also acknowledge use of the Materials Research Science and Engineering Center Biosynthesis facility, supported by grant NSF-MRSEC-1420382. Z.D., W.S., and U.R. acknowledge travel support from the Bronfman Foundation.

REFERENCES

1. Berg, H. 2000. Motile behavior of bacteria. *Phys. Today.* 53:24–29.
2. Calladine, C. R. 1975. Construction of bacterial flagella. *Nature.* 255:121–124.
3. Asakura, S. 1970. Polymerization of flagellin and polymorphism of flagella. *Adv. Biophys.* 1:99–155.
4. Hasegawa, K., I. Yamashita, and K. Namba. 1998. Quasi- and nonequivalence in the structure of bacterial flagellar filament. *Biophys. J.* 74:569–575.
5. Hyman, H. C., and S. Trachtenberg. 1991. Point mutations that lock *Salmonella typhimurium* flagellar filaments in the straight right-handed

and left-handed forms and their relation to filament superhelicity. *J. Mol. Biol.* 220:79–88.

6. Kamiya, R., S. Asakura, …, K. Namba. 1979. Transition of bacterial flagella from helical to straight forms with different subunit arrangements. *J. Mol. Biol.* 131:725–742.
7. Trachtenberg, S., and D. J. DeRosier. 1991. A molecular switch: subunit rotations involved in the right-handed to left-handed transitions of *Salmonella typhimurium* flagellar filaments. *J. Mol. Biol.* 220:67–77.
8. Darnton, N. C., and H. C. Berg. 2007. Force-extension measurements on bacterial flagella: triggering polymorphic transformations. *Biophys. J.* 92:2230–2236.
9. Srigiriraju, S. V., and T. R. Powers. 2005. Continuum model for polymorphism of bacterial flagella. *Phys. Rev. Lett.* 94:248101.
10. Barry, E., Z. Hensel, …, R. Oldenbourg. 2006. Entropy-driven formation of a chiral liquid-crystalline phase of helical filaments. *Phys. Rev. Lett.* 96:018305.
11. Trachtenberg, S., and I. Hammel. 1992. The rigidity of bacterial flagellar filaments and its relation to filament polymorphism. *J. Struct. Biol.* 109:18–27.
12. Hoshikawa, H., and R. Kamiya. 1985. Elastic properties of bacterial flagellar filaments. II. Determination of the modulus of rigidity. *Biophys. Chem.* 22:159–166.
13. Selinger, J. V., and R. F. Bruinsma. 1991. Hexagonal and nematic phases of chains. I. Correlation functions. *Phys. Rev. A.* 43:2910–2921.
14. Strey, H. H., V. A. Parsegian, and R. Podgornik. 1997. Equation of state for DNA liquid crystals: fluctuation enhanced electrostatic double layer repulsion. *Phys. Rev. Lett.* 78:895–898.
15. Maki-Yonekura, S., K. Yonekura, and K. Namba. 2010. Conformational change of flagellin for polymorphic supercoiling of the flagellar filament. *Nat. Struct. Mol. Biol.* 17:417–422.
16. Steiner, A., P. Szekely, …, U. Raviv. 2012. Entropic attraction condenses like-charged interfaces composed of self-assembled molecules. *Langmuir.* 28:2604–2613.
17. Needleman, D. J., M. A. Ojeda-Lopez, …, C. R. Safinya. 2004. Synchrotron x-ray diffraction study of microtubules buckling and bundling under osmotic stress: a probe of interprotofilament interactions. *Phys. Rev. Lett.* 93:198104.
18. Needleman, D. J., M. A. Ojeda-Lopez, …, C. R. Safinya. 2005. Radial compression of microtubules and the mechanism of action of taxol and associated proteins. *Biophys. J.* 89:3410–3423.
19. Szekely, P., R. Asor, …, U. Raviv. 2012. Effect of temperature on the interactions between dipolar membranes. *J. Phys. Chem. B.* 116:3519–3524.
20. Cohen, J. A., R. Podgornik, …, V. A. Parsegian. 2009. A phenomenological one-parameter equation of state for osmotic pressures of PEG and other neutral flexible polymers in good solvents. *J. Phys. Chem. B.* 113:3709–3714.
21. Li, Y., R. Beck, …, M. Divinagracia. 2008. Scatterless hybrid metal-single-crystal slit for small-angle x-ray scattering and high-resolution x-ray diffraction. *J. Appl. Crystallogr.* 41:1134–1139.
22. Nadler, M., A. Steiner, …, U. Raviv. 2011. Following the structural changes during zinc-induced crystallization of charged membranes using time-resolved solution x-ray scattering. *Soft Matter.* 7:1512–1523.
23. Van Vaerenbergh, P., J. Léonardon, …, T. Narayanan. 2016. An upgrade beamline for combined wide, small and ultra small-angle x-ray scattering at the ESRF. *AIP Conf. Proc*. 1741:030034.
24. Ben-Nun, T., A. Ginsburg, …, U. Raviv. 2010. *X+*: a comprehensive computationally accelerated structure analysis tool for solution x-ray scattering from supramolecular self-assemblies. *J. Appl. Crystallogr.* 43:1522–1531.
25. Székely, P., A. Ginsburg, …, U. Raviv. 2010. Solution x-ray scattering form factors of supramolecular self-assembled structures. *Langmuir.* 26:13110–13129.
26. Ben-Nun, T., A. Barak, and U. Raviv. 2016. Spline-based parallel nonlinear optimization of function sequences. *J. Parallel Distrib. Comput.* 93–94:132–145.
27. Ben-Nun, T., R. Asor, …, U. Raviv. 2016. Solution x-ray scattering form-factors with arbitrary electron density profiles and polydispersity distributions. *Isr. J. Chem.* 56:622–628.
28. Ginsburg, A., T. Ben-Nun, …, U. Raviv. 2016. Reciprocal grids: a hierarchical algorithm for computing solution x-ray scattering curves from supramolecular complexes at high resolution. *J. Chem. Inf. Model.* 56:1518–1527.
29. Mimori-Kiyosue, Y., F. Vonderviszt, …, K. Namba. 1996. Direct interaction of flagellin termini essential for polymorphic ability of flagellar filament. *Proc. Natl. Acad. Sci. USA.* 93:15108–15113.
30. Yonekura, K., S. Maki-Yonekura, and K. Namba. 2003. Complete atomic model of the bacterial flagellar filament by electron cryomicroscopy. *Nature.* 424:643–650.
31. Hamilton, W. C. 1974. International Tables for X-ray Crystallography, Vol. IV. Kynoch Press, Birmingham, United Kingdom. (Present distributor Kluwer Academic, Dordrecht, the Netherlands). 273–284.
32. Marsh, R., and K. Slagle. 1983. Corrections to table 2.2 B of volume IV of international tables for x-ray crystallography. *Acta Crystallogr. A.* 39:173.
33. Svergun, D. I., C. Barberato, and M. H. J. Koch. 1995. CRYSOL-a program to evaluate x-ray solution scattering of biological macromolecules from atomic coordinates. *J. Appl. Crystallogr.* 28:768–773.
34. Koutsioubas, A., and J. Pérez. 2013. Incorporation of a hydration layer in the "dummy atom" *ab initio* structural modelling of biological macromolecules. *J. Appl. Crystallogr.* 46:1884–1888.
35. Schneidman-Duhovny, D., M. Hammel, …, A. Sali. 2013. Accurate SAXS profile computation and its assessment by contrast variation experiments. *Biophys. J.* 105:962–974.
36. Fraser, R., T. MacRae, and E. Suzuki. 1978. An improved method for calculating the contribution of solvent to the x-ray diffraction pattern of biological molecules. *J. Appl. Crystallogr.* 11:693–694.
37. Slater, J. C. 1964. Atomic radii in crystals. *J. Chem. Phys.* 41:3199–3204.
38. Roberson, R. E., and R. Schwertassek. 1988. Dynamics of Multibody Systems, Vol. 18. Springer-Verlag, Berlin, Germany.
39. Ben-Shaul, A. 2013. Entropy, energy, and bending of DNA in viral capsids. *Biophys. J.* 104:L15–L17.
40. Yamashita, I., K. Hasegawa, …, K. Namba. 1998. Structure and switching of bacterial flagellar filaments studied by x-ray fiber diffraction. *Nat. Struct. Biol.* 5:125–132.
41. Onsager, L. 1949. The effects of shape on the interaction of colloidal particles. *Ann. N. Y. Acad. Sci.* 51:627–659.
42. Fraden, S., G. Maret, …, R. B. Meyer. 1989. Isotropic-nematic phase transition and angular correlations in isotropic suspensions of tobacco mosaic virus. *Phys. Rev. Lett.* 63:2068–2071.
43. Wensink, H., and G. Vroege. 2003. Isotropic–nematic phase behavior of length-polydisperse hard rods. *J. Chem. Phys.* 119:6868–6882.
44. Stroobants, A., H. Lekkerkerker, and T. Odijk. 1986. Effect of electrostatic interaction on the liquid crystal phase transition in solutions of rodlike polyelectrolytes. *Macromolecules.* 19:2232–2238.
45. Warren, B. 1941. X-ray diffraction in random layer lattices. *Phys. Rev.* 59:693.
46. Leikin, S., V. A. Parsegian, …, R. P. Rand. 1993. Hydration forces. *Ann. Rev. Phys. Chem.* 44:369–395.
47. Israelachvili, J. N. 2011. Intermolecular and Surface Forces, *3rd ed.*. Academic Press, New York.
48. Gittes, F., B. Mickey, …, J. Howard. 1993. Flexural rigidity of microtubules and actin filaments measured from thermal fluctuations in shape. *J. Cell Biol.* 120:923–934.
49. Odijk, T. 1983. The statistics and dynamics of confined or entangled stiff polymers. *Macromolecules.* 16:1340–1344.
50. Odijk, T. 1986. Theory of lyotropic polymer liquid crystals. *Macromolecules.* 19:2313–2329.
51. Dijkstra, M., D. Frenkel, and H. N. Lekkerkerker. 1993. Confinement free energy of semiflexible polymers. *Physica A.* 193:374–393.

52. Danino, D., E. Kesselman, …, D. Harries. 2009. Osmotically induced reversible transitions in lipid-DNA mesophases. *Biophys. J.* 96: L43–L45.

53. Grason, G. M. 2015. Colloquium: geometry and optimal packing of twisted columns and filaments. *Rev. Mod. Phys.* 87:401.

54. Yamashita, I., F. Vonderviszt, …, K. Namba. 1991. Preparing well-oriented sols of straight bacterial flagellar filaments for x-ray fiber diffraction. *J. Mol. Biol.* 217:293–302.

55. Yamashita, I., F. Vonderviszt, …, K. Namba. 1995. Radial mass analysis of the flagellar filament of *Salmonella*: implications for the subunit folding. *J. Mol. Biol.* 253:547–558.

56. Yamashita, I., H. Suzuki, and K. Namba. 1998. Multiple-step method for making exceptionally well-oriented liquid-crystalline sols of macromolecular assemblies. *J. Mol. Biol.* 278:609–615.

57. Safinya, C. R., J. Deek, …, Y. Li. 2013. Liquid crystal assemblies in biologically inspired systems. *Liq. Cryst.* 40:1748–1758.

Biophysical Journal, Volume *112*

Supplemental Information

Structure and Intermolecular Interactions between *L*-Type Straight Flagellar Filaments

Daniel Louzon, Avi Ginsburg, Walter Schwenger, Tom Dvir, Zvonimir Dogic, and Uri Raviv

Structure and Intermolecular Interactions between L-type Straight Flagellar Filaments

D. Louzon, [*,†] A. Ginsburg, [*,‡] W. Schwenger, [§] T. Dvir, [*,†] Z. Dogic, [§] and U. Raviv [*]

[*] The Institute of Chemistry and the Center for Nanoscience and Nanotechnology, The Hebrew University of Jerusalem, Jerusalem, 91904, Israel. [†]The Racah Institute of Physics, The Hebrew University of Jerusalem, Jerusalem, 91904, Israel. [‡]The Institute for drug research, The Hebrew University of Jerusalem. [§] Department of Physics, Brandeis University, Waltham, MA 02454, USA.

SUPPORTING MATERIALS

1 Solvent subtraction

Fig. S1 shows that using Eq. 4 to subtract the displaced volume of the solvent did not improve the fit to our data. Hence Eq. 2 was used in subsequent models.

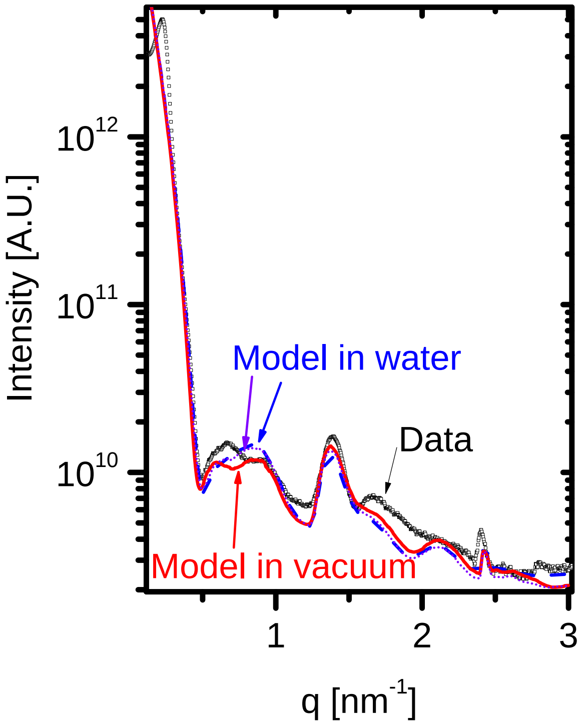

Figure S1: Radially integrated scattering intensity from SJW1660 strain (empty square symbols) and the computed form-factor of a flagella filament, averaged over all orientations in $\vec{q}$-space, using Eqs.2 and 7 (red solid curve) and after taking into account the contribution of the displaced solvent, using Eq. 7 and Eq. 4 with solvent mean electron density of $\rho_0 = 333\, {}^{e}/_{\mathrm{nm}^3}$ (blue broken curve) or with $\rho_0 = 303\, {}^{e}/_{\mathrm{nm}^3}$ (dotten violet curve).

0006-3495/08/09/2624/12 $2.00

2 Varying form-factor parameters

The flagella model (Fig. 3) is supported by the following considerations. The helical character of the structure is supported by looking at the aligned sample shown in Fig. 9. In this figure, the form factor features are governed by the helical shape of the filament at $q > 1\,\mathrm{nm}^{-1}$, indicating that the subunit packing must be considered in the form-factor model. Figs. S2-S4 show the high sensitivity of the calculated form-factor model to small changes in the helix diameter (Fig. S2), the helical pitch (Fig. S3), and the filament tilt angle (Fig. S4).

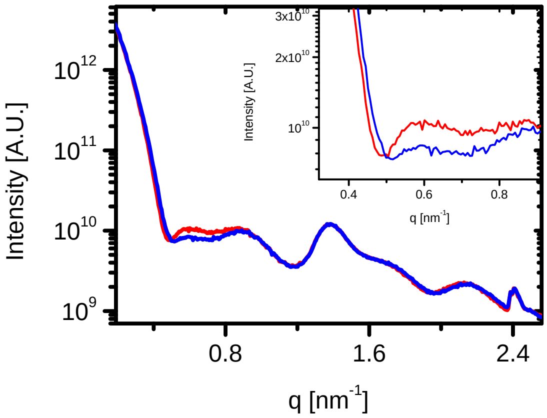

Figure S2: A comparison between two form-factor models with a $0.1\,\mathrm{nm}$ difference in the helix diameter. The main differences between the two models are the location of the first minimum and the amplitude of the following local maximum. The inset, shows these features on an expanded scale.

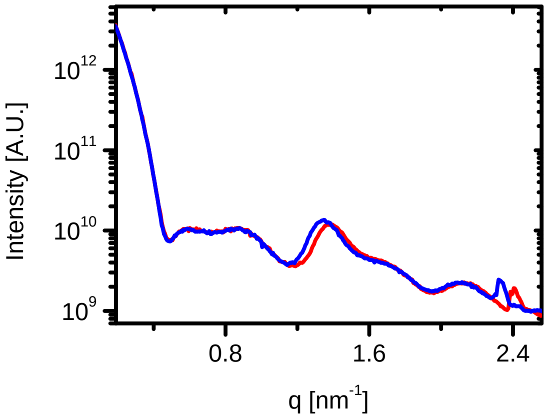

Figure S3: A comparison between two form-factor models with a $0.2\,\mathrm{nm}$ difference in the size of the two turn pitch. The main difference between the two models is the shift of the two layer-line peaks at $q \simeq 1.4\,\mathrm{nm}^{-1}$ and $q \simeq 2.4\,\mathrm{nm}^{-1}$.

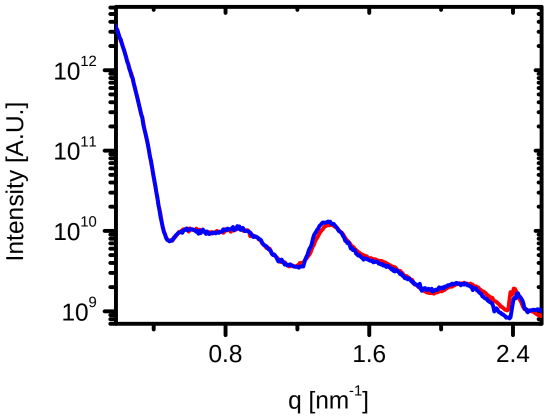

Figure S4: A comparison between two form-factor models with a 1° difference in the angle of the filament tilt. The tilt angle mainly changes the separation between the two layer-line peaks at $q \simeq 1.4\,\mathrm{nm}^{-1}$ and $q \simeq 2.4\,\mathrm{nm}^{-1}$.

Figs. S2-S4 clearly show that each of these parameters predominantly affects different features in the form-factor, allowing them to be optimized (or fit) independently. This fact increase our confidence level in the model.

Fig. S5 shows the calculated $I(q)$ derived from the model of flagellar filaments, arranged in a hexagonal lattice with no thermal fluctuations. The lattice-sum peaks dominates this model and there are almost no form-factor features at $q > \sim 0.5\,\mathrm{nm}^{-1}$.

3 Instrument resolution function

Fig. S5 shows that the intensity of the flagellar bundle model has sharp correlation peaks that were invisible in the SAXS results (Fig. 5). We attribute this observation to the resolution function of our measurement setups, defined by the monochromator, detector pixel size, beam size, sample-to-detector distance, etc. To account for these effects, each of the calculated model intensities was convoluted with a Gaussian function with a standard deviation, $\sigma = 0.03\,\mathrm{nm}^{-1}$, which is the measured resolution of our setup. Fig. S5 (red curve) shows that fewer measurable peaks are expected when the resolution function is taken into account.

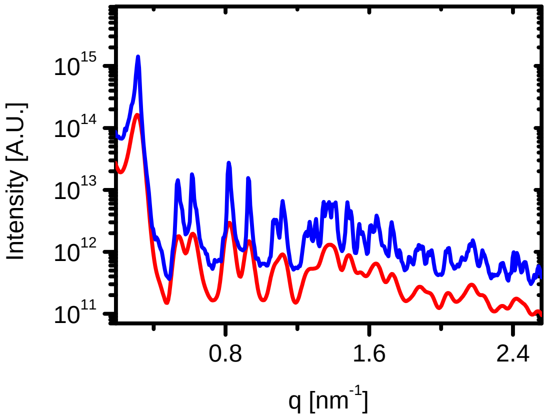

Figure S5: The calculated intensity (as a function of q) of a 15×15 bundle of filaments in a hexagonal lattice with no fluctuations(blue curve). The red curve results from the a convolution between the blue curve and a Gaussian resolution function with a standard deviation of $\sigma = 0.03\,\mathrm{nm}^{-1}$.

4 Varying Structure-factor parameters

The SAXS results (Fig. 5) show that both the structure factor peaks and the form-factor principle features can be observed. Fig. S6 compares between the calculated intensity models of flagellar filament hexagonal bundles with different degrees of thermal fluctuations. The extent of fluctuations was determined by the elastic constant between neighbours', κ, which determines the lattice-sum contribution to the calculated intensity. A sufficiently high κ value, significantly limits thermal fluctuations and the intensity resembles the calculated intensity assuming no thermal fluctuations (Fig. S5, blue curve). If, however, the value of κ is too low, the hexagonal lattice is unstable and the lattice-sum peaks become unclear (Fig. S6, blue curve).

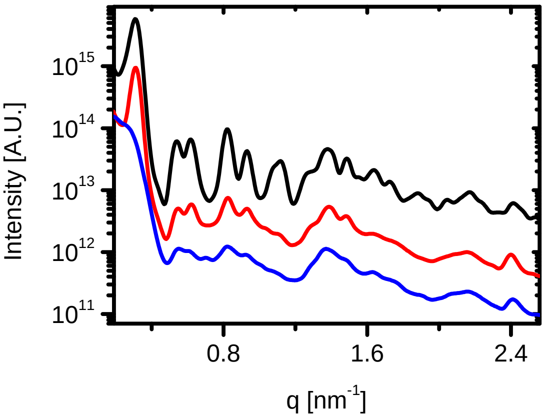

Figure S6: A comparison between the lattice sum contribution to the calculated intensity of three models with different κ values. $\kappa = 8\,\mathrm{mN}\cdot\mathrm{m}^{-1}$ (black curve), $\kappa = 0.8\,\mathrm{mN}\cdot\mathrm{m}^{-1}$ (red curve), and $\kappa = 0.08\,\mathrm{mN}\cdot\mathrm{m}^{-1}$ (blue curve).

The hexagonal lattice constant, a, affects the location of the peaks in the calculated intensity. Fig. S7 shows models with a small difference in the value of a. The figure clearly shows that the model is very sensitive to the value of a, hence a can be accurately determined.

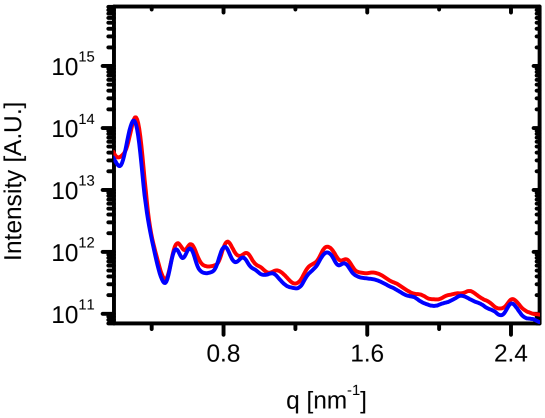

Figure S7: A comparison between the calculated scattering intensities of two models of bundles with a small difference in their lattice constants. The blue curve is with $a = 23.4\,\mathrm{nm}$ and the red curve with $a = 23.8\,\mathrm{nm}$. As the lattice constant increases the correlation peaks shift to lower q values.

Fig. 8 shows how the calculated intensity, $I(q)$, is affected by the size of the bundle. Here the main feature that is affected is the width of the peaks. To clearly see that, the results before and after applying the convolution with the experimental resolution function are shown.

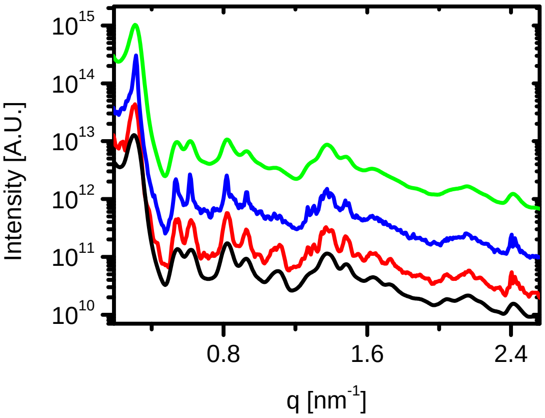

Figure S8: A comparison between the calculated intensity of two models with different sizes of bundles. The red curve corresponds to a bundle of 6×6. The blue curve corresponds to a bundle of 15×15. The difference in the width of the peaks is less clear after applying the resolution function (black for the 6×6 bundle and green for the 15×15 bundle) Note that after applying the resolution function, in the smaller bundle model the peaks at high q and are more distinct.

Unlike the form-factor parameters, the lattice-sum parameters are more dependent of each other and it is possible to attain similar fits by fine tuning κ or the bundle size. These parameters should therefore be considered more carefully. It is, however, clear that the model provides the correct order of magnitude of these parameters.

5 Osmotic stress experiments

Fig. S9 provides additional SAXS curves from flagellar bundles formed under different osmotic pressures, as in Fig. 5.

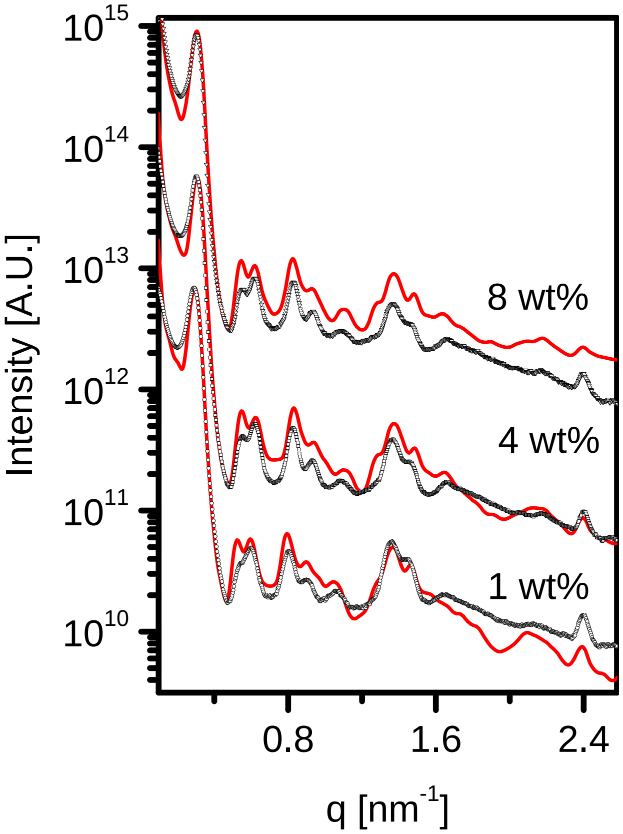

Figure S9: Additional SAXS measurements of SJW1660 in 100 mM NaCl and $10\,\mathrm{mM}$ K_2HPO_4 under different PEG ($M_w = 20,000\,\mathrm{Da}$) concentrations (in $\mathrm{wt}\%$), as indicated (black symbols) with the corresponding computed models (red curve).

6 Equation of state

The equation-of-states for a bundle of long semi-flexible chains in solution is:

$$\frac{\partial G}{\partial d}(d) = \frac{\partial H_0}{\partial d}(d) + ck_BT\kappa_s^{-\frac{1}{4}}\frac{\partial}{\partial d}\sqrt[4]{\frac{\partial^2 H_0}{\partial d^2}} \tag{1}$$

where G is the free energy, $d = a - D$ is the spacing between filaments, κ_s is the bending stiffness, H_0 is:

$$H_0(d) = a_h\frac{e^{-d/\lambda_H}}{\sqrt{d/\lambda_H}} + b\frac{e^{-d/\lambda_D}}{\sqrt{d/\lambda_D}}, \tag{2}$$

where λ_H and λ_D are the hydration and electrostatic screening lengths. The first derivative of H_0 is:

$$\frac{\partial H_0}{\partial d}(d) = -\frac{a_h\left(\frac{2d}{\lambda_H}+1\right)\mathrm{e}^{-\frac{d}{\lambda_H}}}{2\lambda_H\left(\frac{d}{\lambda_H}\right)^{\frac{3}{2}}} - \frac{b\left(\frac{2d}{\lambda_D}+1\right)\mathrm{e}^{-\frac{d}{\lambda_D}}}{2\lambda_D\left(\frac{d}{\lambda_D}\right)^{\frac{3}{2}}} \tag{3}$$

and its second derivative is:

$$\frac{\partial^2 H_0}{\partial d^2}(d) = \frac{a_h\left(\frac{4d^2}{\lambda_H}+4d+3\lambda_H\right)\mathrm{e}^{-\frac{d}{\lambda_H}}}{4\lambda_H^3\left(\frac{d}{\lambda_H}\right)^{\frac{5}{2}}} + \frac{b\left(\frac{4d^2}{\lambda_D}+4d+3\lambda_D\right)\mathrm{e}^{-\frac{d}{\lambda_D}}}{4\lambda_D^3\left(\frac{d}{\lambda_D}\right)^{\frac{5}{2}}} \tag{4}$$

The last term of the equation of state is then:

$$\frac{\partial}{\partial d}\sqrt[4]{\frac{\partial^2 H_0}{\partial d^2}} = -\frac{(\alpha+\beta)\,\mathrm{e}^{-\frac{d}{\lambda_H}-\frac{d}{\lambda_D}}}{\gamma} \tag{5}$$

where

$$\alpha = \left(\frac{d}{\lambda_H}\right)^{\frac{7}{2}} \left(8b\lambda_H^6 d^3 + 12b\lambda_D\lambda_H^6 d^2 + 18b\lambda_D^2\lambda_H^6 x + 15b\lambda_D^3\lambda_H^6\right)\mathrm{e}^{\frac{d}{\lambda_H}} \tag{6}$$

$$\beta = \left(\frac{d}{\lambda_D}\right)^{\frac{7}{2}} \left(8a\lambda_D^6 d^3 + 12a_h\lambda_D^6\lambda_H d^2 + 18a_h\lambda_D^6\lambda_H^2 d + 15a_h\lambda_D^6\lambda_H^3\right)\mathrm{e}^{\frac{d}{\lambda_D}} \tag{7}$$

and

$$\gamma = 32\lambda_D^6\lambda_H^6\left(\frac{d}{\lambda_D}\right)^{\frac{7}{2}}\left(\frac{d}{l}\right)^{\frac{7}{2}}\left(\frac{a_h\left(\frac{4d^2}{\lambda_H}+4d+3\lambda_H\right)\mathrm{e}^{-\frac{d}{\lambda_H}}}{4\lambda_H^3\left(\frac{d}{\lambda_H}\right)^{\frac{5}{2}}} + \frac{b\left(\frac{4d^2}{\lambda_D}+4d+3\lambda_D\right)\mathrm{e}^{-\frac{d}{\lambda_D}}}{4\lambda_D^3\left(\frac{d}{\lambda_D}\right)^{\frac{5}{2}}}\right)^{\frac{3}{4}} \tag{8}$$

In a hexagonal lattice, the relation between the free energy and the osmotic pressure is:

$$-\frac{\partial G}{\partial d}(d) = \sqrt{3}\Pi d. \tag{9}$$